# Modelling laminar transport phenomena in a Casson rheological fluid from a horizontal circular cylinder with partial slip

**Abstract**

The laminar boundary layer flow and heat transfer of Casson non-Newtonian fluid from a permeable horizontal cylinder in the presence of thermal and hydrodynamic slip conditions is analysed. The cylinder surface is maintained at a constant temperature. The boundary layer conservation equations, which are parabolic in nature, are normalised into *non-similar* form and then solved numerically with the well-tested, efficient, implicit, stable Keller–Box finite-difference scheme. Increasing velocity slip induces acceleration in the flow near the cylinder surface and the reverse effect further from the surface. Increasing velocity slip consistently enhances temperatures throughout the boundary layer regime. An increase in thermal slip parameter strongly decelerates the flow and also reduces temperatures in the boundary layer regime. An increase in Casson rheological parameter acts to elevate considerably the skin friction (non-dimensional wall shear stress) and this effect is pronounced at higher values of tangential coordinate. Temperatures are however very slightly decreased with increasing values of Casson rheological parameter. Increasing mass flow injection (blowing) at the cylinder surface causes a strong acceleration, whereas increasing suction is found to induce the opposite effect. The study finds applications in rheological chocolate food processing.

**Keywords**

Non-Newtonian fluid mechanics, Casson model, yield stress, slip condition, Keller–Box numerical method, heat transfer, skin friction, Nusselt number, boundary layers, chocolate food processing

## Introduction

Non-Newtonian transport phenomena arise in many branches of process mechanical, chemical and materials engineering. Such fluids exhibit shear stress–strain relationships, which diverge significantly from the classical Newtonian (Navier–Stokes) model. Most non-Newtonian models involve some form of modification to the momentum conservation equations. These include power-law fluids,[1] viscoelastic fluids including Maxwell upper-convected models,[2] Walters-B short memory models,[3,4] Oldroyd-B models,[5] differential Reiner–Rivlin models[6,7] and Bingham plastics.[8] The flow of non-Newtonian fluids in the presence of heat transfer is an important research area due to its relevance to the optimised processing of chocolate,[9] toffee and other foodstuffs.[10] Of the various rheological models developed in biotechnology and food engineering, the Casson model has proved very successful. This simple, yet elegant rheological model was introduced originally[11] to simulate industrial inks. This model[12] constitutes a plastic fluid model which exhibits shear thinning characteristics, yield stress and high shear viscosity. The Casson fluid model is reduced to a Newtonian fluid at a very high wall shear stress i.e. when the wall stress is much greater than yield stress. This fluid model also approximates reasonably well the rheological behaviour of other liquids including physiological suspensions, foams, cosmetics, syrups, etc.

A number of theoretical, numerical and experimental studies of transport phenomena in Casson fluids

have been presented in a variety of areas including biomedical engineering[13–15] and manufacturing technology.[16] Neofytou[17] studied computationally the flow characteristics of both power-law and Casson fluids in symmetric sudden expansions, showing that the critical generalised Reynolds number of transition from symmetry to asymmetry and subsequently the inverse dimensionless wall shear stress are linearly related to the dimensionless wall shear rate. Kandasamy et al.[18] numerically studied the thermal convection in concentric annuli using a Casson model. Mass transfer in a Casson flowing through an annular geometry was examined by Nagarani et al.[19] who derived analytical solutions and also considered boundary absorption effects. Hemodynamic simulations of Casson blood flow in complex arterial geometries were studied by Gorla et al.[20] and Murthy and Pradhan.[21] Attia and Sayed-Ahmed[22] studied the unsteady hydromagnetic Couette flow and heat transfer in a Casson fluid using the Crank–Nicolson implicit method, showing that Casson number (dimensionless yield stress parameter) controls strongly the velocity overshoot and has a significant effect on the time at which the overshoot arises. Hayat et al.[23] obtained homotopic solutions for stagnation-point flow and heat transfer of a Casson fluid along a stretching surface, also considering viscous heating effects. Mustafa et al.[24] very recently investigated also with a homotopy method, the transient dissipative flow and heat transfer of a Casson fluid over a moving flat plate with a parallel free stream, showing that surface shear stress and surface heat transfer are increased with the Casson fluid parameter and also Eckert number (viscous heating parameter).

The above studies invariably assumed the 'no-slip' condition at the boundary. Slip effects have, however, shown to be significant in certain industrial thermal problems and manufacturing fluid dynamics systems. Sparrow et al.[25] presented the first significant investigation of laminar slip-flow heat transfer for tubes with uniform heat flux. Inman[26] further described the thermal convective slip flow in a parallel plate channel or a circular tube with uniform wall temperature. These studies generally indicated that velocity slip acts to enhance heat transfer whereas thermal slip (or 'temperature jump') depresses heat transfer.

Many studies have appeared in recent years considering both hydrodynamic and thermal slip effects. Interesting articles of relevance to process mechanical engineering include Larrode et al.[27] who studied thermal/velocity slip effects in conduit thermal convection, Spillane[28] who examined sheet processing boundary layer flows with slip boundary conditions and Crane and McVeigh[29] who studied slip hydrodynamics on a micro-scale cylindrical body. Further studies in the context of materials processing include Ameel et al.,[30] Yu and Ameel,[31] Crane and McVeigh.[32] Studies of slip flows from curved bodies include Bég et al.[33] who examined using network numerical simulation the magneto-convective slip flow from a rotating disk, Wang and Ng[34] who studied using asymptotic analysis the slip hydrodynamics from a stretching cylinder. Wang[35] has also examined stagnation slip flow and heat transfer from an axially moving cylinder showing that heat transfer increases with slip, Prandtl number and Reynolds number, and that in the case of large slip, the flow field decays exponentially into potential flow.

The objective of the present paper is to investigate the laminar boundary layer flow and heat transfer of a Casson rheological fluid past a horizontal cylinder. Mathematical modelling through equations of continuity and motion leads to dimensionless non-linear coupled differential boundary layer equations. The velocity and thermal slip conditions along with conservation law of mass, momentum and energy completes the problems formulation for velocity components and temperature. The considered slip conditions are important in non-Newtonian foodstuff transport processes,[10,12] which often exhibit wall slip. It has been experimentally verified that fluid possesses non-continuum features such as slip flow when the molecular mean free path length of fluid is comparable to a representative geometrical length of the system being studied e.g. diameter of a cylindrical body. A finite difference numerical solution is presented for the transformed boundary layer equations and a parametric study is conducted the Prandtl number, Casson rheological parameter, wall suction/injection and velocity/thermal slip effects on the momentum and heat transfer characteristics conducted. The present problem has to the authors' knowledge not appeared thus far in the scientific literature.

## Mathematical flow model

Consider the steady, laminar, two-dimensional, viscous, incompressible, buoyancy-driven convection heat transfer flow from a horizontal permeable circular cylinder embedded in a Casson non-Newtonian fluid. Figure 1 shows the flow model and physical coordinate system. The $x$-coordinate is measured along the circumference of the horizontal cylinder from the lowest point and the $y$-coordinate is measured normal to the surface, with '$a$' denoting the radius of the horizontal cylinder. $\Phi = x/a$ is the angle of the $y$-axis with respect to the vertical ($0 \leqslant \Phi \leqslant \pi$). The gravitational acceleration, $\boldsymbol{g}$ acts downwards. Both the horizontal cylinder and the fluid are maintained initially at the same temperature. Instantaneously they are raised to a temperature $T_w > T_\infty$ the ambient temperature of the fluid which remains unchanged. The rheological equation of state for an isotropic flow of Casson fluid, following Steffe[10] in tensorial notation may be stated as

$$\tau_{ij} = \begin{cases} 2\left(\mu_B + \frac{p_y}{\sqrt{2\pi}}\right)e_{ij}, & \pi \geqslant \pi_c \\ 2\left(\mu_B + \frac{p_y}{\sqrt{2\pi_c}}\right)e_{ij}, & \pi < \pi_c \end{cases} \tag{1}$$

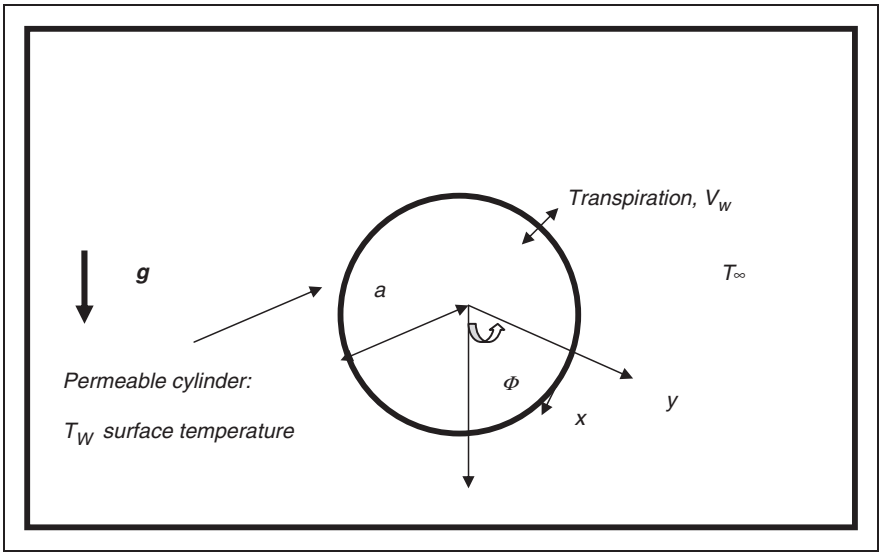


**Figure 1.** Physical model and coordinate system.

in which $\pi = e_{ij}e_{ij}$ and $e_{ij}$ is the $(i,j)$th component of deformation rate, $\pi$ denotes the product of the component of deformation rate with itself, $\pi c$ shows a critical value of this product based on the non-Newtonian model, $\mu_B$ the plastic dynamic viscosity of non-Newtonian fluid and $p_y$ is the yield stress of fluid. In line with the approach of Yih[36] and introducing the boundary layer approximations, the governing conservation equations can be written as follows

$$\frac{\partial u}{\partial x} + \frac{\partial v}{\partial y} = 0 \tag{2}$$

$$u\frac{\partial u}{\partial x} + v\frac{\partial u}{\partial y} = g\Lambda(T - T_\infty)\sin\left(\frac{x}{a}\right) + \nu\left(1 + \frac{1}{\beta}\right)\frac{\partial^2 u}{\partial y^2} \tag{3}$$

$$u\frac{\partial T}{\partial x} + v\frac{\partial T}{\partial y} = \alpha\frac{\partial^2 T}{\partial y^2} \tag{4}$$

Where $u$ and $v$ are the velocity components in the $x$- and $y$-directions, respectively, $\nu$, the kinematic viscosity of the fluid, $\beta$, the non-Newtonian Casson parameter, $\Lambda$, the co-efficient of thermal expansion, $\alpha$, the thermal diffusivity, $T$, the temperature, respectively. The boundary conditions are prescribed at the cylinder surface and the edge of the boundary layer regime (free stream), respectively as follows

$$\begin{aligned} &y = 0, \quad u = N_0\left(1 + \frac{1}{\beta}\right)\frac{\partial u}{\partial y}, v = -V_w, \quad T = T_w + K_0\frac{\partial T}{\partial y} \\ &y \to \infty, \quad u \to 0, \; T \to T_\infty \end{aligned} \tag{5}$$

in which $N_0$ is the velocity slip factor and $K_0$ is the thermal slip factor. For $N_0$=0=$K_0$, one can recover the classical *no-slip* case.

The stream function $\psi$ is defined by $u = \partial\psi/\partial y$ and $v = \partial\psi/\partial x$ and therefore, the continuity equation (2) is automatically satisfied. In order to write the governing equations and the boundary conditions in dimensionless form, the following non-dimensional quantities are introduced.

$$\begin{aligned} &\xi = \frac{x}{a}, \quad \eta = \frac{y}{a}\sqrt[4]{Gr}, \quad f(\xi,\eta) = \frac{\psi}{\nu\xi\sqrt[4]{Gr}}, \quad \Pr = \frac{\nu}{\alpha} \\ &\theta(\xi,\eta) = \frac{T - T_\infty}{T_w - T_\infty}, \quad Gr = \frac{g\Lambda(T_w - T_\infty)a^3}{\nu^2}, \\ &\beta = \mu_B\frac{\sqrt{2\pi_c}}{p_y} \end{aligned} \tag{6}$$

where, $T_\infty$ is the free stream temperature, and $V_w$ is the uniform blowing/suction velocity.

In view of equation (6), equations (2) to (4) reduce to the following coupled, non-linear, dimensionless partial differential equations for momentum and energy for the regime

$$\left(1 + \frac{1}{\beta}\right)f''' + ff'' - f'^2 + \frac{\sin\xi}{\xi}\theta = \xi\left(f'\frac{\partial f'}{\partial\xi} - f''\frac{\partial f}{\partial\xi}\right) \tag{7}$$

$$\frac{\theta''}{\Pr} + f\theta' = \xi\left(f'\frac{\partial f'}{\partial\xi} - f''\frac{\partial f}{\partial\xi}\right) \tag{8}$$

The transformed dimensionless boundary conditions are

$$\begin{aligned} &\text{At } \eta = 0, \quad f = S, \quad f' = \left(1 + \frac{1}{\beta}\right)S_f f''(0), \\ &\theta = 1 + S_T\theta'(0) \\ &\text{As } \eta \to \infty, \quad f' \to 0, \quad \theta \to 0 \end{aligned} \tag{9}$$

In the above equations, the primes denote the differentiation with respect to $\eta$, the dimensionless radial coordinate, $\xi$, the dimensionless tangential coordinate, $\Phi$, the azimuthal coordinate, $Gr$, the Grashof (free convection) parameter, $\Pr = \frac{\nu}{\alpha}$, the Prandtl number, $S_f = \frac{N_0 Gr^{1/4}}{a}$ and $S_T = \frac{K_0 Gr^{1/4}}{a}$, the

non-dimensional velocity slip and thermal slip parameters, respectively and $f_w = \frac{-V_w a}{\nu \sqrt[4]{Gr}}$, the blowing/suction parameter ($f_w < 0$ for $V_w > 0$ (the case of blowing), and $f_w > 0$ for $V_w < 0$ (the case of suction)). Of course the special case of a *solid cylinder surface* corresponds to $f_w = 0$.

The engineering design quantities of physical interest include the skin-friction coefficient and Nusselt number, which are given by

$$\frac{1}{2} C_f Gr^{-3/4} = \left(1 + \frac{1}{\beta}\right) \xi f''(0) \tag{10}$$

$$\frac{Nu}{\sqrt[4]{Gr}} = -\theta'(0) \tag{11}$$

## Numerical solution

In this study, the efficient Keller–Box implicit difference method has been employed to solve the general flow model defined by equations (7) and (8) with boundary conditions (9). This method was originally developed for low speed aerodynamic boundary layers by Keller,[37] and has been employed in a diverse range of industrial multi-physical fluid dynamics problems. These include cross-diffusion boundary layer flows,[38] radiative-convective hydromagnetic flow from curved bodies in porous media,[39,40] heat and mass transfer in non-linear porous media,[41] micropolar convection,[42] nanofluid dynamics,[43,44] chemically reactive double-diffusive convection[45] and unsteady viscoelastic flow and mass diffusion.[46] The fundamental phases intrinsic to the Keller–Box scheme are:

(a) Reduction of the *N*th order partial differential equation system to *N* first-order equations
(b) Finite difference discretisation
(c) Quasilinearisation of non-linear Keller algebraic equations
(d) Block-tridiagonal elimination of linear Keller algebraic equations

### *Phase a: Reduction of the Nth order partial differential equation system to N first-order equations*

Equations (7) and (8) subject to the boundary conditions (9) are first written as a system of first-order equations. For this purpose, we reset equations (7) and (8) as a set of simultaneous equations by introducing the new variables $u$, $v$ and $t$

$$f' = u \tag{12}$$

$$f'' = v \tag{13}$$

$$\theta' = t \tag{14}$$

$$\left(1 + \frac{1}{\beta}\right) v' + fv - u^2 + \frac{\sin \xi}{\xi} \theta = \xi \left( u \frac{\partial u}{\partial \xi} - v \frac{\partial f}{\partial \xi} \right) \tag{15}$$

$$\frac{1}{\Pr} t' + ft = \xi \left( u \frac{\partial s}{\partial \xi} - t \frac{\partial f}{\partial \xi} \right) \tag{16}$$

where primes denote differentiation with respect to $\eta$.

In terms of the dependent variables, the boundary conditions become

$$\begin{aligned} &\text{At } \eta = 0: \quad u = \left(1 + \frac{1}{\beta}\right) f''(0), \quad f = f_w, \quad s = 1 \\ &\text{As } \eta \to \infty: \quad u \to 0, \quad s \to 0 \end{aligned} \tag{17}$$

### *Phase b: Finite difference discretisation*

A two-dimensional computational grid is imposed on the $\xi$-$\eta$ plane as sketched in Figure 2. The stepping process is defined by

$$\eta_0 = 0, \ \eta_j = \eta_{j-1} + h_j, \quad j = 1, 2, \ldots, J, \ \eta_J \equiv \eta_\infty \tag{18}$$

$$\xi^0 = 0, \ \xi^n = \xi^{n-1} + k_n, \ n = 1, 2, \ldots, N \tag{19}$$

where $k_n$ and $h_j$ denote the step distances in the $\xi$ and $\eta$ directions, respectively.

If $g_j^n$ denotes the value of any variable at $(\eta_j, \xi^n)$, then the variables and derivatives of equations (12) to (16) at $\left(\eta_{j+1/2}, \xi^{n-1/2}\right)$ are replaced by

$$g_{j-1/2}^{n-1/2} = \frac{1}{4} \left( g_j^n + g_{j-1}^n + g_j^{n-1} + g_{j-1}^{n-1} \right) \tag{20}$$

$$\left( \frac{\partial g}{\partial \eta} \right)_{j-1/2}^{n-1/2} = \frac{1}{2h_j} \left( g_j^n - g_{j-1}^n + g_j^{n-1} - g_{j-1}^{n-1} \right) \tag{21}$$

$$\left( \frac{\partial g}{\partial \xi} \right)_{j-1/2}^{n-1/2} = \frac{1}{2k^n} \left( g_j^n - g_{j-1}^n + g_j^{n-1} - g_{j-1}^{n-1} \right) \tag{22}$$

We now state the finite-difference approximation of equations (12) to (16) for the *mid-point* $\left(\eta_{j-1/2}, \xi^n\right)$

$$h_j^{-1} \left( f_j^n - f_{j-1}^n \right) = u_{j-1/2}^n, \tag{23}$$

$$h_j^{-1} \left( u_j^n - u_{j-1}^n \right) = v_{j-1/2}^n, \tag{24}$$

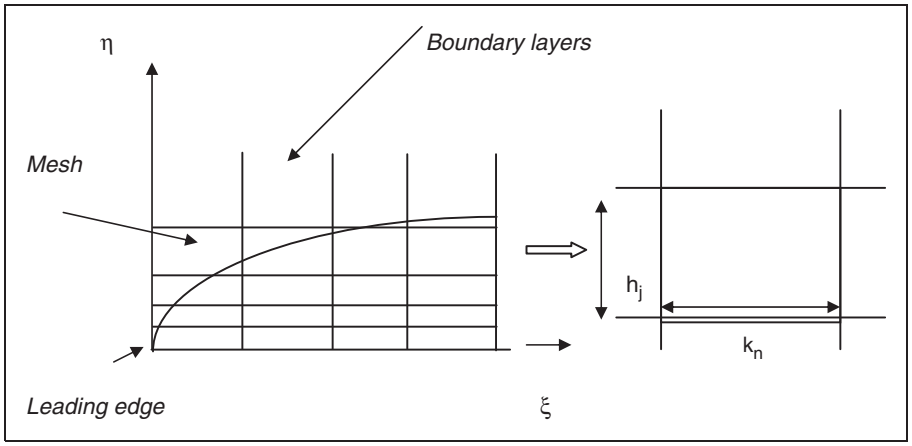


**Figure 2.** Grid meshing and a Keller–Box computational cell.

$$\left(1+\frac{1}{\beta}\right)(v_j - v_{j-1}) + \frac{(1+\alpha)h_j}{4} \times \left[(f_j + f_{j-1})(v_j + v_{j-1})\right] - \frac{h_j}{4}(1+\alpha)(u_j + u_{j-1})^2 + \frac{\alpha h_j}{2} v_{j-1/2}^{n-1}(f_j + f_{j-1}) - \frac{\alpha h_j}{2} f_{j-1/2}^{n-1}(v_j + v_{j-1}) + \frac{Bh_j}{2}(s_j + s_{j-1}) = [R_1]_{j-1/2}^{n-1} \quad (25)$$

$$h_j^{-1}\left(\theta_j^n - \theta_{j-1}^n\right) = t_{j-1/2}^n \quad (26)$$

$$\frac{1}{\mathrm{Pr}}(t_j - t_{j-1}) + \frac{(1+\alpha)h_j}{4}\left[(f_j + f_{j-1})(t_j + t_{j-1})\right] - \frac{\alpha h_j}{4}\left[(u_j + u_{j-1})(s_j + s_{j-1})\right] + \frac{\alpha h_j}{2} s_{j-1/2}^{n-1}(u_j + u_{j-1}) - \frac{\alpha h_j}{2} u_{j-1/2}^{n-1}(s_j + s_{j-1}) - \frac{\alpha h_j}{2} f_{j-1/2}^{n-1}(t_j + t_{j-1}) + \frac{\alpha h_j}{2} t_{j-1/2}^{n-1}(f_j + f_{j-1}) = [R_2]_{j-1/2}^{n-1} \quad (27)$$

where we have used the abbreviations

$$\alpha = \frac{\xi^{n-1/2}}{k_n}, \quad B = \frac{\sin\left(\xi^{n-1/2}\right)}{\xi^{n-1/2}} \quad (28)$$

$$[R_1]_{j-1/2}^{n-1} = -h_j\left[\left(1+\frac{1}{\beta}\right)\left(\frac{v_j - v_{j-1}}{h_j}\right) + (1-\alpha)\left(f_{j-1/2} v_{j-1/2}\right) + (\alpha - 1)\left(u_{j-1/2}\right)^2 + B\left(s_{j-1/2}\right)\right] \quad (29)$$

$$[R_2]_{j-1/2}^{n-1} = -h_j\left[\frac{1}{\mathrm{Pr}}\left(\frac{t_j - t_{j-1}}{h_j}\right) + (1-\alpha)\left(f_{j-1/2} t_{j-1/2}\right) + \alpha\left(u_{j-1/2} s_{j-1/2}\right)\right] \quad (30)$$

The boundary conditions are

$$f_0^n = u_0^n = 0, \quad \theta_0^n = 1, \quad u_J^n = 0, \quad \theta_J^n = 0 \quad (31)$$

### *Phase c: Quasilinearisation of non-linear Keller algebraic equations*

If we assume $f_j^{n-1}$, $u_j^{n-1}$, $v_j^{n-1}$, $s_j^{n-1}$, $t_j^{n-1}$ to be known for $0 \leqslant j \leqslant J$, equations (23) to (27) are a system of $5J+5$ equations for the solution of $5J+5$ unknowns $f_j^n$, $u_j^n$, $v_j^n$, $p_j^n$, $s_j^n$, $t_j^n$, $j = 0,1,2,\ldots,J$. This non-linear system of algebraic equations is *linearised* by means of Newton's method as explained in Keller,[37] Prasad et al.,[38–40] Vasu et al.[41] and Anwar Bég et al.[42,43]

### *Phase d: Block-tridiagonal elimination of linear Keller algebraic equations*

The linear system (23) to (27) can now be solved by the *block-elimination* method, since they possess a *block-tridiagonal* structure. Commonly, the block-tridiagonal structure consists of variables or constants, but here, an interesting feature can be observed, namely that it consists of *block matrices*. The complete linearised system is formulated as a *block matrix system*, where each element in the coefficient matrix is a matrix itself. Then, this system is solved using the efficient Keller–Box method. The numerical results are affected by the number of mesh points in both directions. After some trials in the $\eta$-direction (radial coordinate) a larger number of mesh points are selected whereas in the $\xi$ direction (tangential coordinate) significantly less mesh points are utilised. $\eta_{\max}$ has been set at 10 and this defines an adequately large value at which the prescribed boundary conditions are satisfied. $\xi_{\max}$ is set at 3.0 for this flow domain. *Mesh independence* is therefore achieved in the present computations. The computer program of the algorithm is executed in MATLAB running on a PC. The method demonstrates excellent stability, convergence and consistency, as elaborated by Keller.[37]

## Results and discussions

In order to verify the accuracy of our present method, we have compared our results with those of Merkin[47] and Yih.[36] Table 1 shows the comparisons of the values of $-\theta'(\xi,0)$, $\beta \to \infty, f_w = 0, N_0 = 0, K_0 = 0$.

Comprehensive solutions have been obtained and are presented in Figures 3 to 20. The numerical problem comprises two independent variables ($\xi$,$\eta$), two dependent fluid dynamic variables ($f$,$\theta$) and six thermo-physical and body force control parameters, namely $Pr, S_f, S_T, \beta, f_w, \xi$. In the present computations, the following default parameters are prescribed (unless otherwise stated): $Pr = 0.71$, $S_f = 0.5$, $S_T = 1.0$, $\beta = 1.0$, $f_w = 0.5$, $\xi = 1.0$. In addition we also consider the effect of *stream wise (transverse) coordinate* location on flow dynamics. The value of the parameter $\xi$ is extremely important. For $\xi \sim 0$, the location is in the vicinity of the *lower stagnation point* on the cylinder. The governing dimensionless equations (7) to (8) in this case reduce to the following ordinary differential equations

$$\left(1+\frac{1}{\beta}\right) f''' + ff'' - f'^2 + \theta = 0 \tag{32}$$

$$\frac{1}{\mathrm{Pr}}\theta'' + f\theta' = 0 \tag{33}$$

since $\frac{\sin\xi}{\xi} \to 0/0$ i.e. 1, so that $\frac{\sin\xi}{\xi}\theta \to \theta$. Another special case arises at $\xi \sim \pi$, which physically corresponds to the *upper stagnation point* on the cylinder surface (diametrically opposite to the lower stagnation point). We note that since the Grashof-free convection parameter, $Gr$, is absorbed into the definitions for radial coordinate ($\eta$) and dimensionless stream function ($f$), it is not considered explicitly in the graphs.

**Table 1.** Values of the local heat transfer coefficient ($Nu$) for various values of $\xi$ with $\beta \to \infty$, $f_w = 0$, $N_0 = 0, K_0 = 0$.

| | $-\theta'(\xi,0)$ | | |
|---|---|---|---|
| $\xi$ | Merkin[47] | Yih[36] | Present results |
| 0·0 | 0.4212 | 0.4214 | 0.4213 |
| 0·2 | 0.4204 | 0.4207 | 0.4206 |
| 0·4 | 0.4182 | 0.4184 | 0.4185 |
| 0·6 | 0.4145 | 0.4147 | 0.4146 |
| 0·8 | 0.4093 | 0.4096 | 0.4095 |
| 1·0 | 0.4025 | 0.4030 | 0.4031 |
| 1·2 | 0.3942 | 0.3950 | 0.3947 |
| 1·4 | 0.3843 | 0.3854 | 0.3857 |
| 1·6 | 0.3727 | 0.3740 | 0.3733 |
| 1·8 | 0.3594 | 0.3608 | 0.3602 |
| 2·0 | 0.3443 | 0.3457 | 0.3458 |
| 2·2 | 0.3270 | 0.3283 | 0.3280 |
| 2·4 | 0.3073 | 0.3086 | 0.3079 |
| 2·6 | 0.2847 | 0.2860 | 0.2858 |
| 2·8 | 0.2581 | 0.2595 | 0.2590 |
| 3·0 | 0.2252 | 0.2267 | 0.2261 |
| $\pi$ | 0.1963 | 0.1962 | 0.1961 |

In Figures 3 and 4, the influence of velocity slip parameter on velocity and temperature distributions is illustrated. Dimensionless velocity component (Figure 3) at the wall is strongly reduced with an increase in slip parameter, $S_f$. There will be a corresponding decrease in the momentum (velocity) boundary layer thickness. The influence of $S_f$ is evidently more pronounced closer to the cylinder surface ($\eta = 0$). Further from the surface, there is a transition in *velocity slip effect*, and the flow is found to be accelerated markedly. Smooth decays of the velocity profiles are observed into the free stream demonstrating excellent convergence of the numerical solution. These trends in the response of velocity field in external thermal convection from a cylinder were also observed by Wang and Ang[34] and Wang.[35] Furthermore the acceleration near the wall with increasing velocity slip effect has been computed by Crane and McVeigh[32] using asymptotic methods, as has the retardation in flow further from the wall. The switch in velocity slip effect on velocity evolution has also been observed for the case of a power-law rheological fluid by Ojadi et al.[48] Figure 4 indicates that an increase in velocity slip parameter significantly enhances temperature in the flow field and thereby increases thermal boundary layer thickness enhances. This will result therefore in the transport of more thermal energy from the cylinder surface to the Casson fluid and will therefore accentuate heat transfer to the fluid, as noted also by Wang.[35] Temperature profiles consistently decay monotonically from a maximum at the cylinder surface to the free stream. All profiles converge at large value of radial coordinate, again showing that convergence has been achieved in the numerical computations. A similar pattern of thermal response to that computed in Figure 4 for a wide range of velocity slip parameters has been noted by Aziz[49] who has indicated also that temperature is enhanced since increasing velocity slip parameter decreases shear stresses and this permits a more effective transfer of heat from the wall to the fluid regime.

In Figures 5 and 6, the variation of velocity and temperature with the transverse coordinate ($\eta$), with increasing thermal slip parameter $S_T$ is depicted. The response of velocity is much more consistent than for the case of changing velocity slip parameter (Figure 3) – it is strongly decreased for all locations in the radial direction. The peak velocity accompanies the case of no thermal slip ($S_T = 0$). The maximum deceleration corresponds to the case of strongest thermal slip ($S_T = 3$). Temperatures (Figure 6) are also strongly depressed with increasing thermal slip. The maximum effect is observed at the wall. Further into the free stream, all temperature profiles converge smoothly

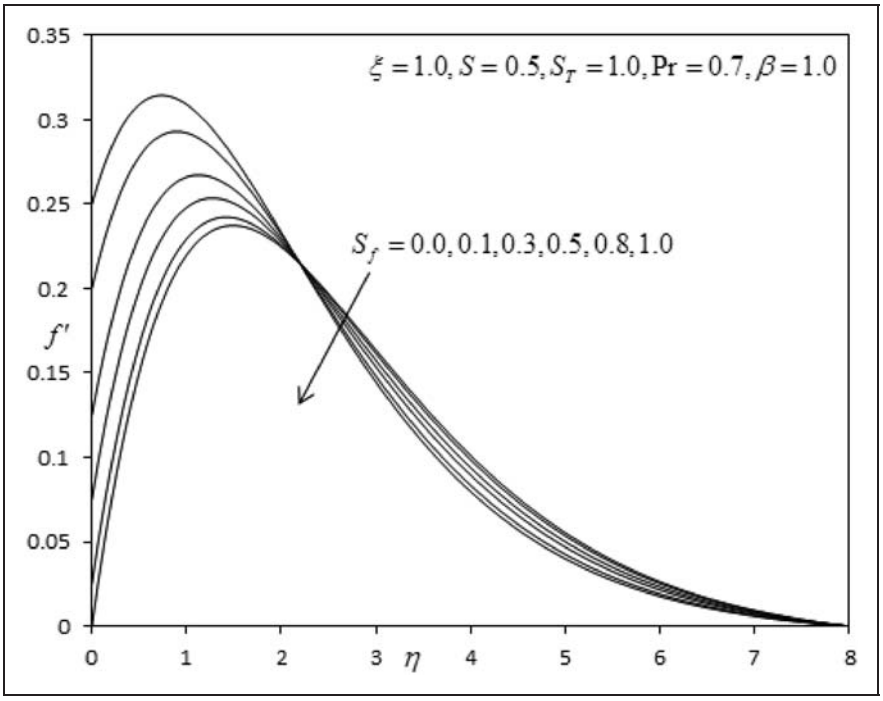


**Figure 3.** Influence of $S_f$ on velocity profiles.

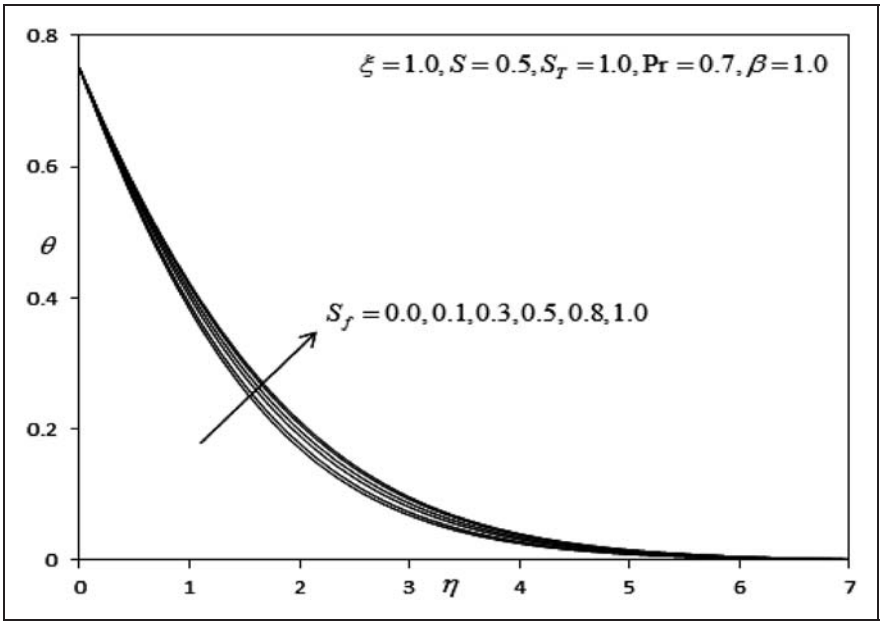


**Figure 4.** Influence of $S_f$ on temperature profiles.

to the vanishing value. The numerical computations correlate well with the results of Larrode et al.[27] who also found that temperature is strongly lowered with increasing thermal slip and that this is attributable to the decrease in heat transfer from the wall to the fluid regime, although they considered only a Newtonian fluid.

In Figures 7 and 8, depict the influence Casson fluid parameter, $\beta$ on velocity and temperature profiles. This parameter features in the shear term in the momentum boundary layer equation (7), and also in the velocity boundary condition (9). For Newtonian flow, yield stress $p_y$ is zero and $\beta = \mu_B\sqrt{\pi_c}/p_y \to \infty$ i.e. the appropriate term in equation (7) reduces from $(1 + 1/\beta)f^{///} \to 1$. Similarly the velocity boundary condition in (9) reduces from $(1 + 1/\beta)\ S_f\ f^{//}(0) \to S_f\ f^{//}(0)$. An increase in $\beta$ implies a decrease therefore in yield stress of the Casson fluid. This effectively facilitates flow of the fluid i.e. accelerates the boundary layer flow close to the cylinder surface, as

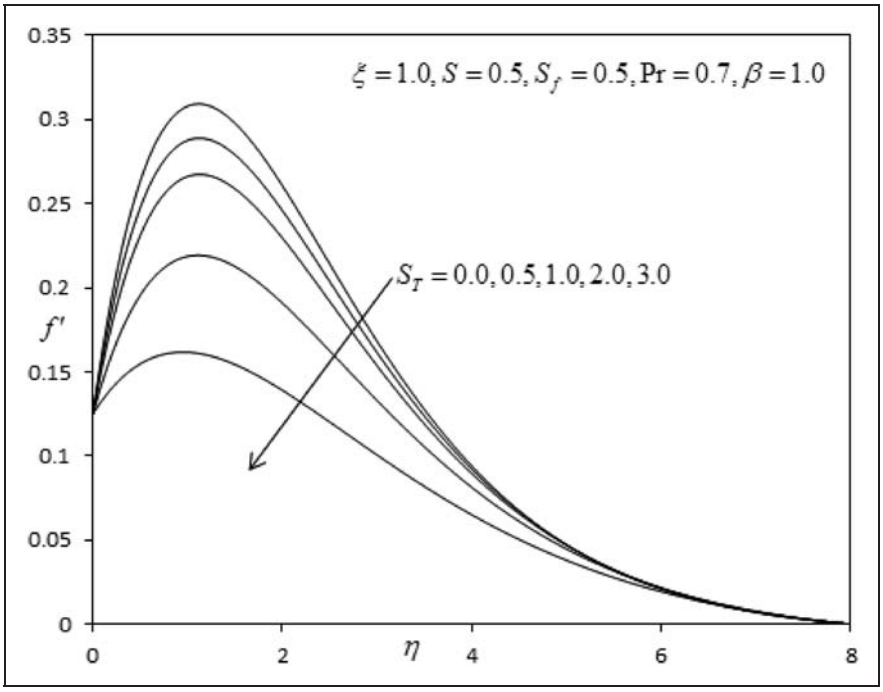


**Figure 5.** Influence of $S_T$ on velocity profiles.

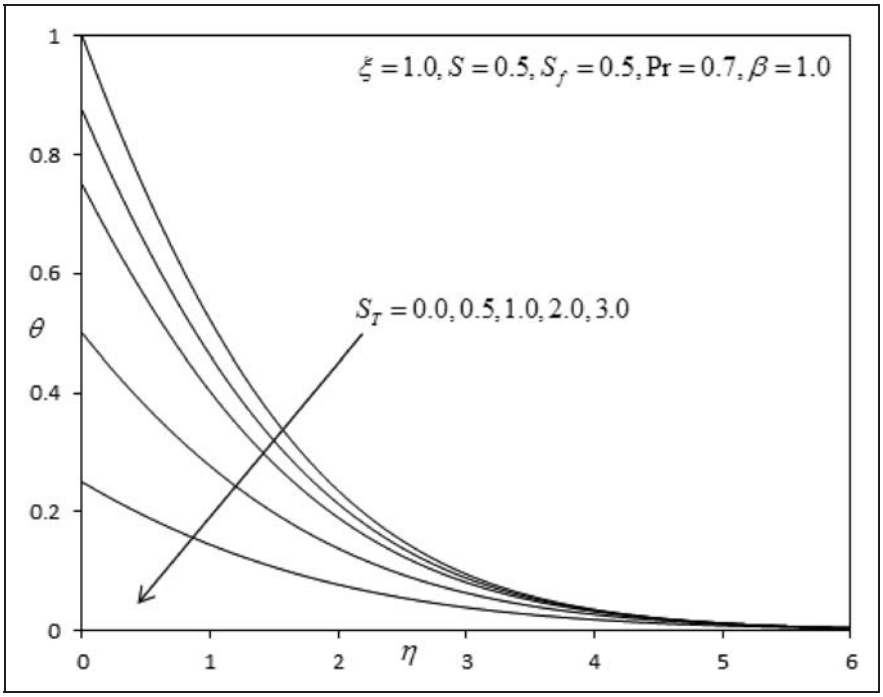


**Figure 6.** Influence of $S_T$ on temperature profiles.

demonstrated by Figure 7. Since the Casson parameter is also present in the wall boundary condition, the acceleration effect is only confined to the region close to the cylinder surface. Further from this zone, the velocity slip factor, $S_f$ will exert a progressively reduced effect and an increase in Casson parameter, $\beta$, will manifest with a deceleration in the flow. Overall, however, the dominant influence of $\beta$, is near the wall and is found to be assistive to momentum development (with larger $\beta$ values the fluid is closer in behaviour to a *Newtonian* fluid and further departs from *plastic* flow) Only a very small decrease in temperature is observed with a large enhancement in Casson fluid parameter, as shown in Figure 8. The Casson parameter does not arise in the thermal boundary layer equation (8), nor does it feature in

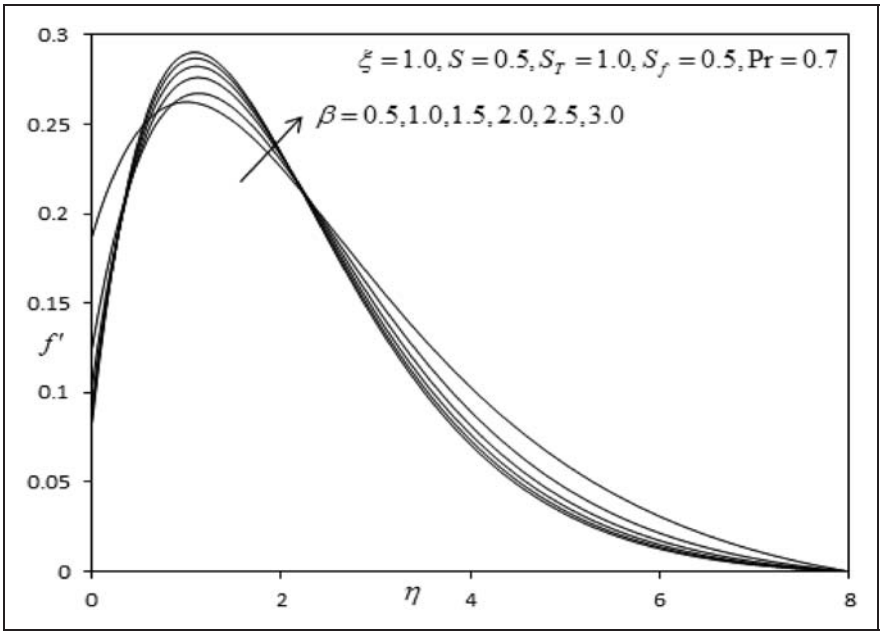


**Figure 7.** Influence of $\beta$ on velocity profiles.

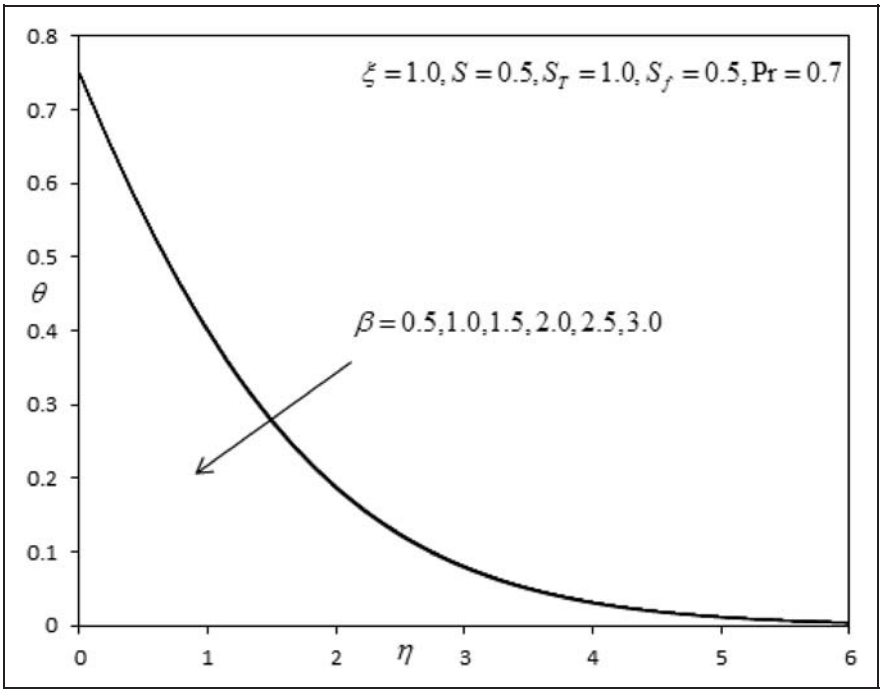


**Figure 8.** Influence of $\beta$ on temperature profiles.

the thermal boundary conditions. The influence on temperature field is therefore experienced indirectly via coupling of the thermal equation (8) with the momentum equation (7). Similar behaviour to the computations shown in Figures 7 and 8, has been observed by Attia and Sayed-Ahmed[27] who also observed acceleration in Casson fluid flow near a curved surface, and additionally by Mustafa et al.[24] who also observed an elevation in velocities near the wall and a slight reduction in temperatures throughout the boundary layer regime.

Figures 9 and 10 present the effect of Prandtl number ($Pr$) on the velocity and temperature profiles along the radial direction, normal to the cylinder surface. Prandtl number embodies the ratio of *viscous diffusion* to *thermal diffusion* in the boundary layer regime. It also expresses the ratio of the *product of specific heat capacity and dynamic viscosity*, to the

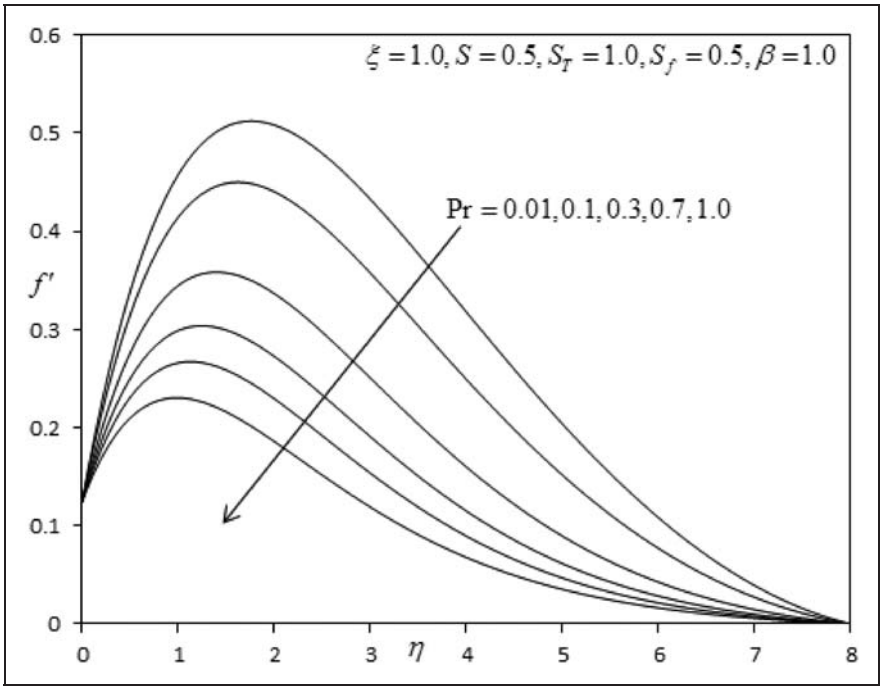


**Figure 9.** Influence of *Pr* on velocity profiles.

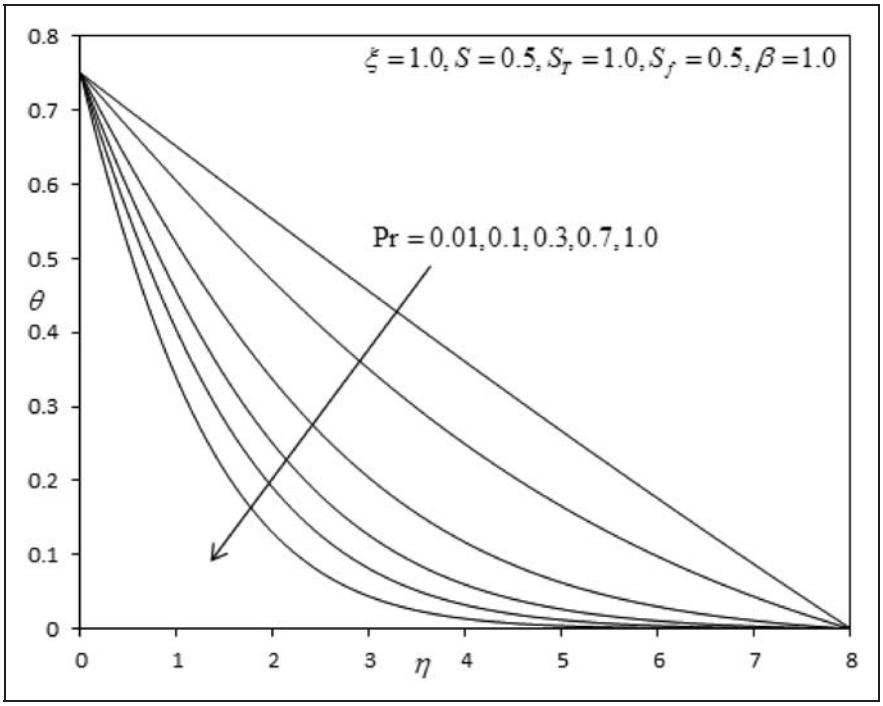


**Figure 10.** Influence of *Pr* on temperature profiles.

*fluid thermal conductivity*. When *Pr* is high, viscous diffusion rate exceeds thermal diffusion rate. An increase in *Pr* from 0.01 through 0.1, 0.3, 0.5, 0.7 to 1.0, is found to significantly depress velocities (Figure 9) and this trend is sustained throughout the regime i.e. for all values of the radial coordinate,$\eta$. For $Pr < 1$, thermal diffusivity exceeds momentum diffusivity i.e. heat will diffuse faster than momentum. Therefore for lower *Pr* fluids (e.g. $Pr = 0.01$ *which physically correspond to liquid metals*), the flow will be accelerates whereas for greater *Pr* fluids (e.g. $Pr = 1$) it will be *strongly decelerated*, as observed in figure. For $Pr = 1.0$, both the viscous and energy diffusion rates will be the same as will the thermal and velocity boundary layer thicknesses. This case can be representative of food stuffs e.g. low-density

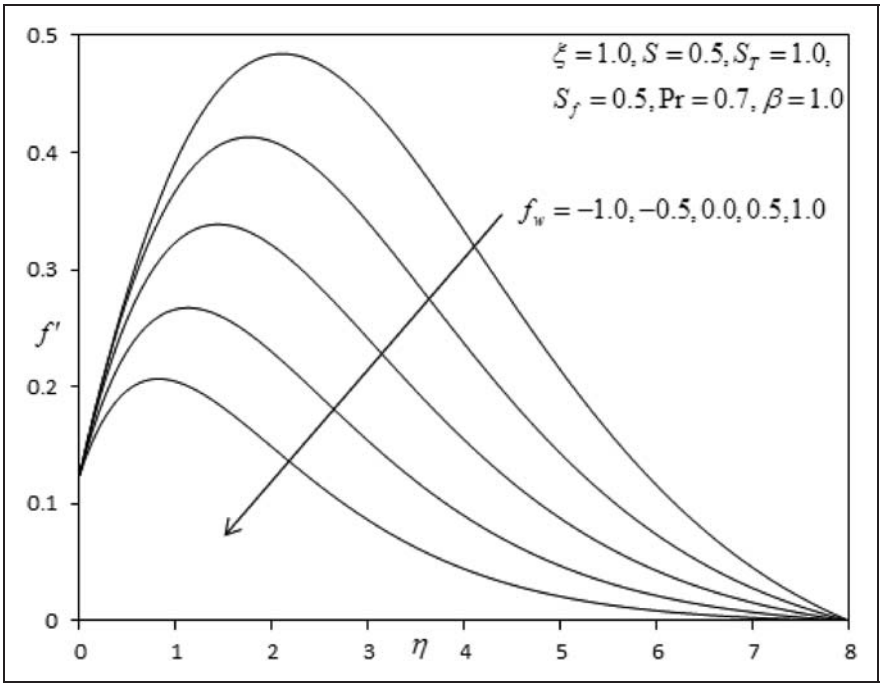


**Figure 11.** Influence of $f_w$ on velocity profiles.

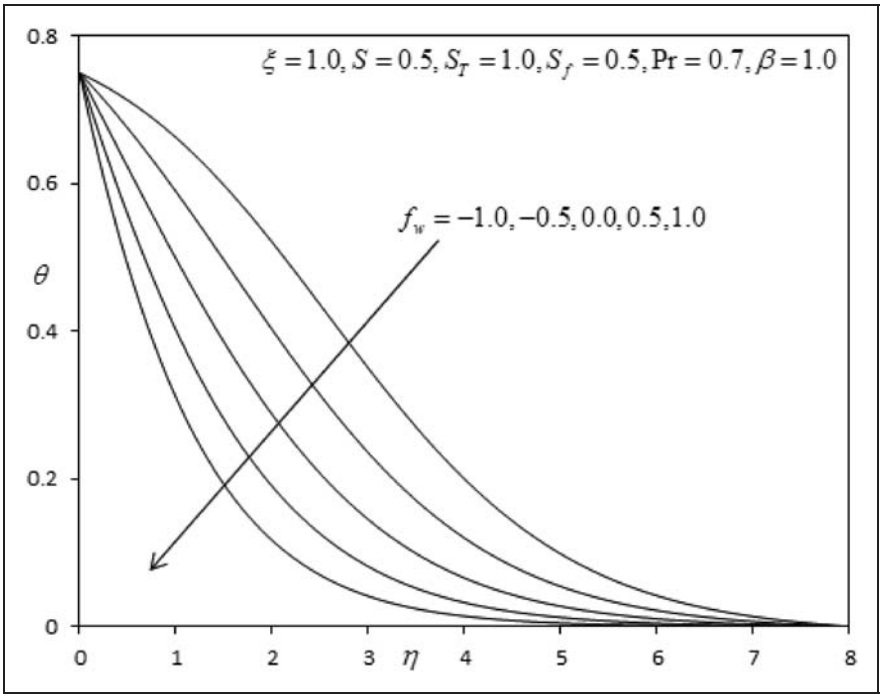


**Figure 12.** Influence of $f_w$ on temperature profiles.

polymorphic forms of chocolate suspensions, as noted by Steffe[10] and Debaste et al.[50] Temperature is found to be strongly reduced with increasing Prandtl number. For the case of $Pr = 0.01$, the decay is almost exactly *linear*. For larger $Pr$ values, the decay is found to be *increasingly monotonic*. Therefore for lower thermal conductivity fluids (as typified by liquid chocolate and other foodstuffs), lower temperatures are observed throughout the boundary layer regime.

Figures 11 and 12 illustrate the influence of wall transpiration on the velocity and temperature functions with radial distance, $\eta$. With an increase in suction ($f_w > 0$) the velocity is clearly decreased i.e. the flow is decelerated. Increasing suction causes the

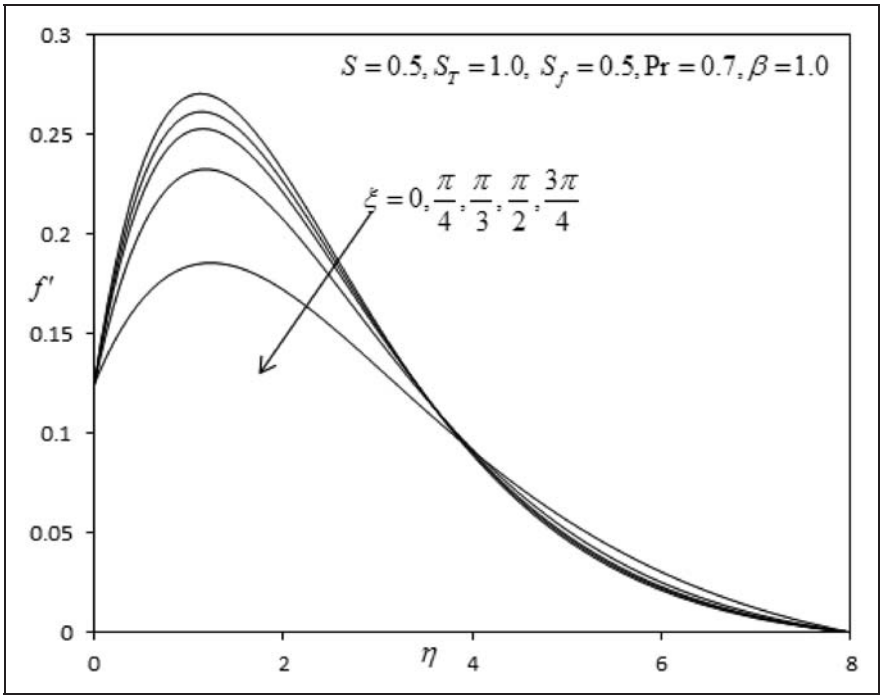


**Figure 13.** Influence of $\xi$ on velocity profiles.

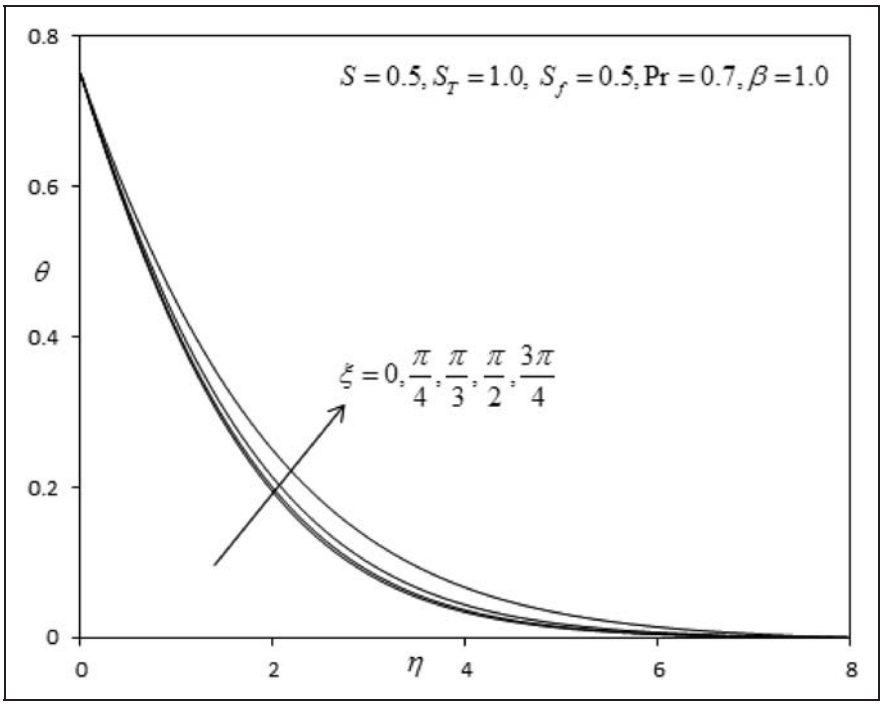


**Figure 14.** Influence of $\xi$ on temperature profiles.

boundary layer to adhere closer to the flow and destroys momentum transfer; it is therefore an excellent control mechanism for stabilising the external boundary layer flow on the circular cylinder. Conversely with increased blowing i.e. injection of fluid via the cylinder surface in to the porous medium regime, ($f_w < 0$), the flow is strongly accelerated i.e. velocities are increased. As anticipated the case of a solid cylinder ($f_w = 0$) falls between the weak suction and weak blowing cases. Peak velocity is located, as in the figures described earlier, at close proximity to cylinder surface. With a decrease in blowing and an increase in suction the peaks progressively displace closer to the cylinder surface, a distinct effect described in detail in

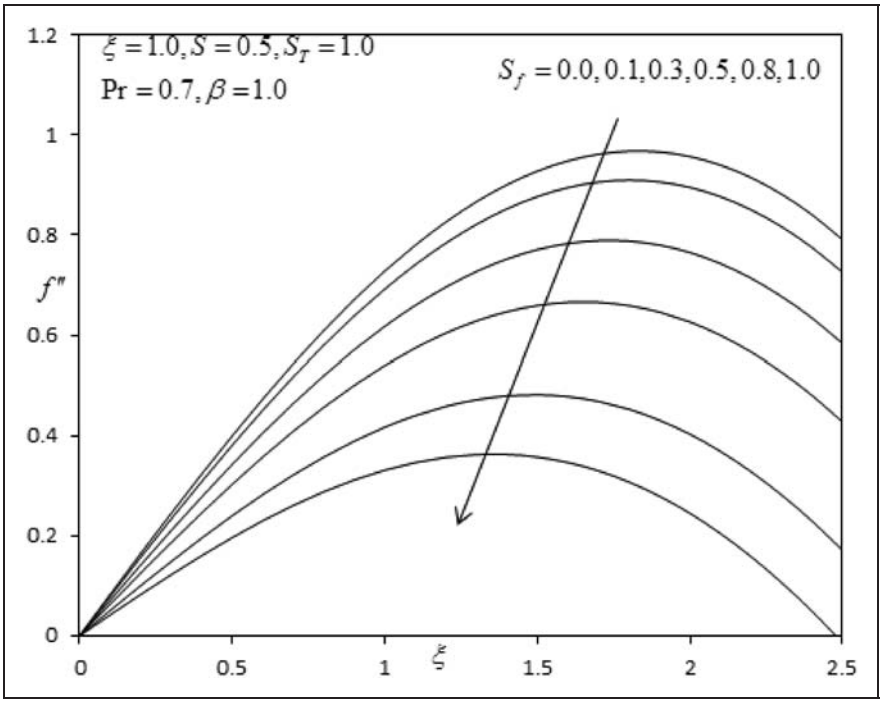


**Figure 15.** Effect of $S_f$ on the skin friction coefficient results.

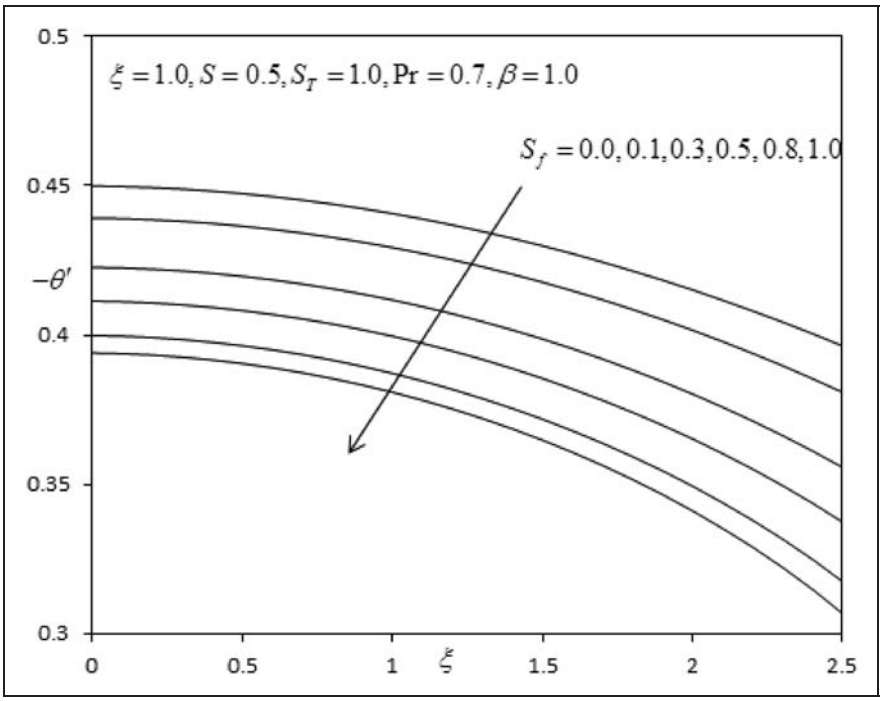


**Figure 16.** Effect of $S_f$ on the local Nusselt number results.

several studies of non-Newtonian boundary layers.[1,3,7,23,24] Temperature, $\theta$, is also elevated considerably with increased blowing at the cylinder surface and depressed with increased suction. The temperature profiles, once again assume a continuous decay from the cylinder surface to the free stream, whereas the velocity field initially ascends, peaks and then decays in to the free stream. The strong influence of wall transpiration (i.e. suction or injection) on boundary layer variables is clearly highlighted. Such a mechanism is greatly beneficial in achieving flow control and regulation of heat and mass transfer characteristics in food processing from a cylindrical geometry.

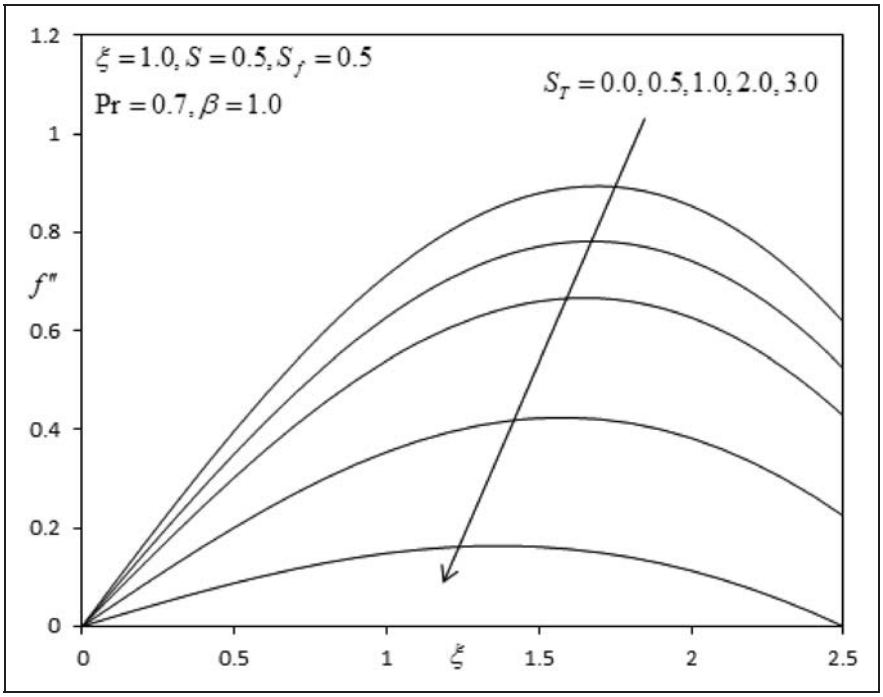


**Figure 17.** Effect of $S_T$ on the skin friction coefficient results.

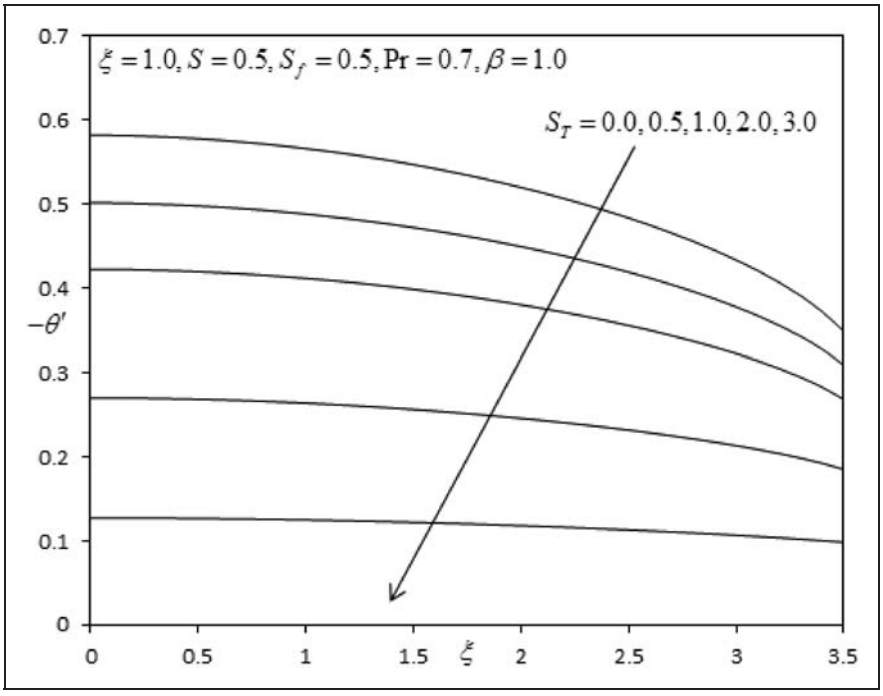


**Figure 18.** Effect of $S_T$ on the local Nusselt number results.

Figures 13 and 14, the variation of velocity and temperature fields with different transverse coordinate, $\xi$, is shown. In the vicinity of the cylinder surface, velocity ($f'$) is found to be maximised closer to the *lower* stagnation point and minimised with progressive distance away from it i.e. the flow is decelerated with increasing $\xi$ However, further from the wall, this trend is reversed and a slight acceleration in the flow is generated with greater distance from the lower stagnation point i.e. velocity values are higher for greater values of $\xi$, as we approach the *upper stagnation point* temperature $\theta$, is found to noticeably increase through the boundary layer with increasing $\xi$ values. Evidently the fluid regime is cooled most efficiently at the lower stagnation point and heated more effectively as we progress around the cylinder periphery upwards

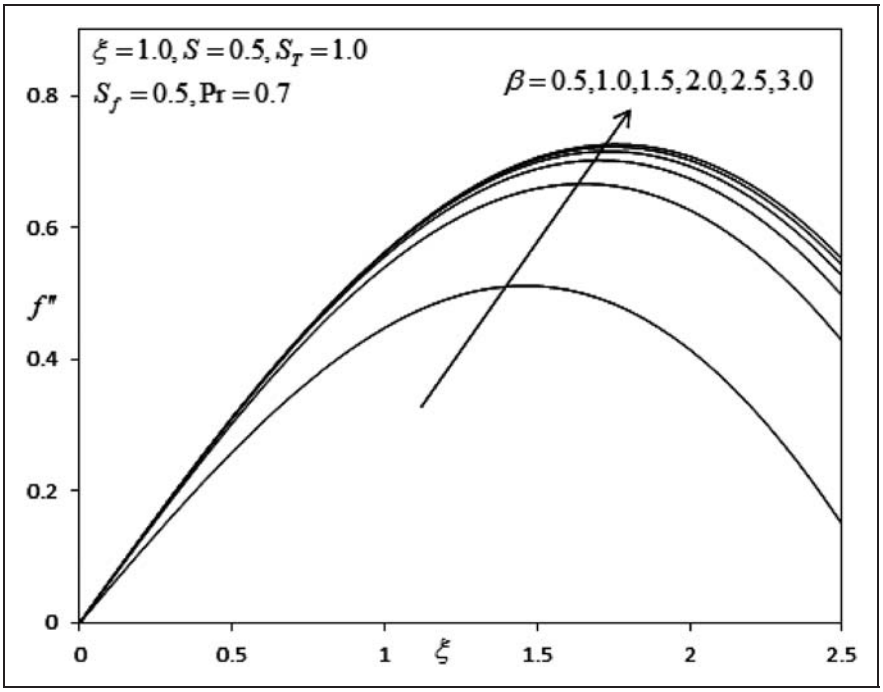


**Figure 19.** Effect of $\beta$ on the skin friction coefficient results.

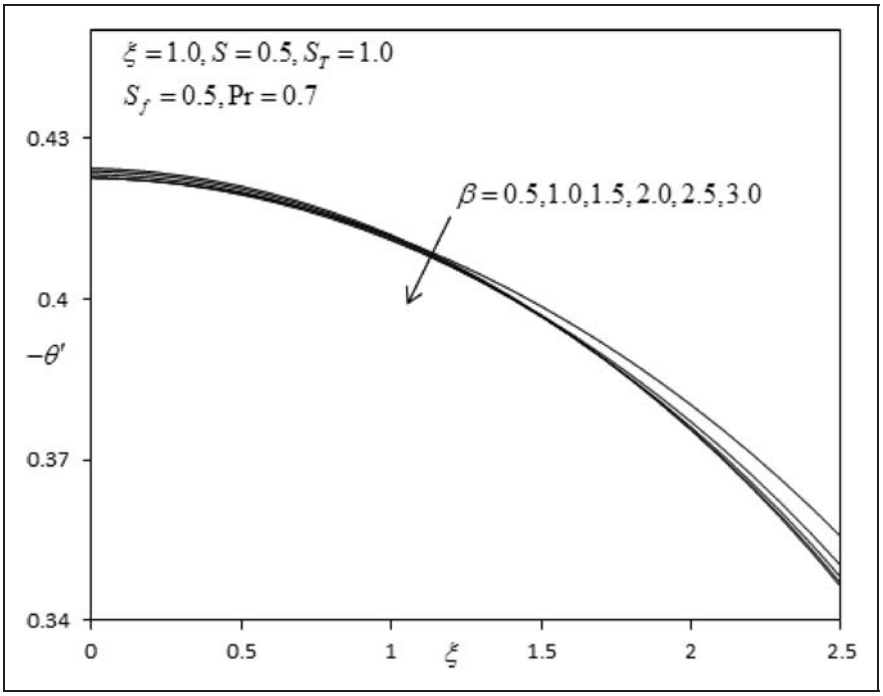


**Figure 20.** Effect of $\beta$ on the local Nusselt number results.

towards the upper stagnation point. These patterns computed for temperature and velocity evolution around the cylinder surface are corroborated with many other studies including work on non-Newtonian Casson fluid convection by Kandasamy et al.[18] and studies of Newtonian convection from a cylinder by Wang[35] and Prasad et al.[40]

Figures 15 and 16 show the effect of velocity slip parameter $S_f$ on cylinder surface shear stress ($f^{//}$) and local Nusselt number ($-\theta^{/}$) variation. In consistency with the earlier graphs described for velocity evolution, with an increase in $S_f$, wall shear stress is consistently reduced i.e. the flow is *decelerated* along the cylinder surface. Again this trend has been observed

by Wang and Ang[34] and Wang[35] using asymptotic methods. There is also a *progressive migration* in the peak shear stress locations further from the *lower stagnation point*, as wall slip parameter is increased. The impact of wall slip is therefore significant on the boundary layer characteristics of Casson flow from a cylinder. With an increasing $S_f$, the local Nusselt number is also considerably decreased and profiles are generally monotonic decays. Maximum local Nusselt number always arises at the cylinder surface and is minimised with proximity to the lower stagnation point i.e. greater distance from the *upper stagnation point*. This pattern of behaviour has also been observed and emphasised by Yih[36] for *Newtonian* flow. In both Figures 15 and 16, skin friction coefficient and local Nusselt number are maximised for the case of no-slip i.e. $S_f = 0$, this result concurring with the analyses of Wang[35] and also Hayat et al.[23]

Figures 17 and 18 show the effect of thermal slip parameter $S_T$ on dimensionless wall shear stress function i.e. skin friction coefficient and local Nusselt number, respectively. Increasing $S_T$ is found to decrease both skin friction coefficient and local Nusselt number. A similar set of profiles is computed as in Figure 15 for velocity distributions, and we observe that with *increasing thermal slip*, peak velocities are displaced *closer* to the lower stagnation point. For lower values of thermal slip, the plots are also similar to those in Figure 16, and have a parabolic nature; however, with $S_T$ values greater than 1, the profiles lose their curvature and become increasingly *linear* in nature. This trend is maximised for the highest value of $S_T$ (=3.0) for which local Nusselt number is found to be almost invariant with transverse coordinate, $\xi$

Figures 19 and 20 illustrate the effect of Casson fluid parameter, $\beta$, on skin friction coefficient and local Nusselt number, respectively. With an increase in $\beta$ the skin friction coefficient increases, since as computed earlier, the flow velocity is enhanced with higher values of $\beta$. Larger $\beta$ values correspond to a progressive decrease in yield stress of the Casson fluid i.e. a reduction in rheological characteristics. With higher $\beta$ the flow approaches closer to *Newtonian* behaviour and the fluid is able to shear faster along the cylinder surface. Local Nusselt number is conversely found to decrease slightly as Casson fluid parameter is increased. This concurs with the earlier computation (Figure 8) on temperature distribution. With increasing $\beta$ values, less heat is transferred from the cylinder surface to the fluid regime, resulting in lower temperatures in the regime external to the cylinder and lower local Nusselt numbers, as observed in Figure 20.

## Conclusions

Numerical solutions have been presented for the transport phenomena i.e. combined heat and flow of Casson rheological fluid external to a horizontal circular cylinder, with suction/injection effects and velocity/thermal slip. The model has been developed to simulate foodstuff transport processes in industrial manufacturing operations. A robust, extensively-validated, implicit finite difference numerical scheme has been implemented to solve the transformed, dimensionless velocity and thermal boundary layer equations, subject to physically realistic boundary conditions. The computations have shown that:

1. Increasing the velocity slip parameter, $S_f$, reduces the velocity near the cylinder surface and also skin friction coefficient and also increases temperature and decreases local Nusselt number.
2. Increasing the thermal slip parameter, $S_T$, decreases velocity and skin friction coefficient and also reduces temperature for all values of radial coordinate i.e. throughout the boundary layer regime, and furthermore decreases local Nusselt number.
3. Increasing the Casson fluid parameter, $\beta$, increases the velocity near the cylinder surface but decreases velocity further from the cylinder, and also fractionally lowers the temperature throughout the boundary layer regime.
4. Increasing the Casson fluid parameter, $\beta$, strongly increases the wall shear stress (skin friction coefficient) and slightly decreases the local Nusselt number, with the latter more significantly affected at large distances from the lower stagnation point i.e. higher values of transverse coordinate.
5. Increasing Prandtl number, $Pr$, decelerates the flow and also strongly depresses temperatures, throughout the boundary layer regime.
6. Increasing suction at the cylinder surface ($f_w > 0$) decelerates the flow whereas increasing injection ($f_w < 0$, i.e. blowing) induces a strong acceleration.
7. Increasing suction at the cylinder surface ($f_w > 0$) reduces temperature whereas increasing injection ($f_w < 0$ i.e. blowing) induces the opposite response and elevates temperature.
8. Increasing transverse coordinate, $\xi$, depresses velocity near the cylinder surface but enhances velocity further from the cylinder, whereas it continuously increases temperature throughout the boundary layer.

The current study has been confined to steady-state flow i.e. ignored transient effects[4] and also neglected thermal radiation heat transfer effects.[39,40] These aspects are also of relevance to rheological food processing simulations and will be considered in future investigations.

### Funding

This research received no specific grant from any funding agency in the public, commercial, or not-for-profit sectors.

## References


1. Anwar Bég O, Abdel Malleque K and Islam MN. Modelling of Ostwald-deWaele non-Newtonian flow over a rotating disk in a non-Darcian porous medium. *Int J Appl Math Mech* 2012; 8: 46–67.
2. Anwar Bég O and Makinde OD. Viscoelastic flow and species transfer in a Darcian high-permeability channel. *J Petrol Sci Eng* 2011; 76: 93–99.
3. Gouse Mohiddin S, Prasad VR and Anwar Bég O. Numerical study of unsteady free convective heat and mass transfer in a Walters-B viscoelastic flow along a vertical cone. *Int J Appl Math Mech* 2010; 6: 88–114.
4. Prasad VR, Vasu B, Anwar Bég O, et al. Unsteady free convection heat and mass transfer in a Walters-B viscoelastic flow past a semi-infinite vertical plate: a numerical study. *Therm Sci Int Scient J* 2011; 15(2): S291–S305.
5. Tripathi D, Anwar Bég O and Curiel-Sosa J. Homotopy semi-numerical simulation of peristaltic flow of generalised Oldroyd-B fluids with slip effects. *Comput Meth Biomech Biomed Eng* 2012; DOI:10.1080/10255842.2012.688109.
6. Anwar Bég O, Takhar HS, Bharagava R, et al. Numerical study of heat transfer of a third grade viscoelastic fluid in non-Darcian porous media with thermophysical effects. *Phys Script* 2008; 77: 1–11.
7. Rashidi MM, Anwar Bég O and Rastegari MT. A study of non-Newtonian flow and heat transfer over a non-isothermal wedge using the homotopy analysis method. *Chem Eng Commun* 2012; 199: 231–256.
8. Huilgol RR and You Z. Application of the augmented Lagrangian method to steady pipe flows of Bingham, Casson and Herschel–Bulkley fluids. *J Non-Newtonian Fluid Mech* 2005; 128: 126–143.
9. Wilson LL, Speers A and Tung MA. Yield stresses in molten chocolates. *J Text Stud* 1993; 24: 269–286.
10. Steffe JF. *Rheological methods in food process engineering*. 2nd ed. Michigan: Freeman Press, 2001.
11. Casson N. A flow equation for pigment oil-suspensions of the printing ink type. In: CC Mill (ed.) *Rheology of disperse systems*. London: Pergamon Press, 1959, p.84.
12. Bird RB, Dai GC and Yarusso BJ. The rheology and flow of viscoplastic materials. *Rev Chem Eng* 1983; 1: 1–83.
13. Chaturani P and Ponnalagarsamy R. Pulsatile flow of Casson's fluid through stenosed arteries with applications to blood flow. *Biorheology* 1986; 23: 499–511.
14. Das B and Batra RL. Secondary flow of a Casson fluid in a slightly curved tube. *Int J Non-Linear Mech* 1995; 28: 567–580.
15. Dash RK, Jayaraman G and Mehta KN. Shear-augmented dispersion of a solute in a Casson fluid flowing in a conduit. *Ann Biomed Eng* 2000; 28: 373–385.
16. Batra RL and Das B. Flow of Casson fluid between two rotating cylinders. *Fluid Dyn Res* 1992; 9: 133–141.
17. Neofytou P. Transition to asymmetry of generalised Newtonian fluid flows through a symmetric sudden expansion. *J Non-Newtonian Fluid Mech* 2006; 133: 132–140.
18. Kandasamy A, Karthik K and Phanidhar PV. Entrance region flow heat transfer in concentric annuli for a Casson fluid. In: *International Conference on Thermal Issues in Emerging Technologies, Theory and Application (ThETA)*, Cairo, Egypt, 3–6 January 2007.
19. Nagarani P, Sarojamma G and Jayaraman G. On the dispersion of a solute in a Casson fluid flow in an annulus with boundary absorption. In: *American Conference on Applied Mathematics (MATH'08)*, Harvard, Massachusetts, USA, 24–26 March 2008, Harvard University, pp.265–273.
20. Shaw S, Gorla RSR, Murthy PVSN, et al. Effect of stenosis on the Casson fluid flow through a bifurcated artery. *Int J Fluid Mech Res* 2009; 36: 43–63.
21. Shaw S, Murthy PVSN and Pradhan SC. The effect of body acceleration on two dimensional flow of Casson fluid through an artery with asymmetric stenosis. *Open Transp Phenom J* 2010; 2: 55–68.
22. Attia H and Sayed-Ahmed ME. Transient MHD Couette flow of a Casson fluid between parallel plates with heat transfer. *Italian J Pure Appl Math* 2010; 27: 19–38.
23. Hayat T, Pop I and Hendi AA. Stagnation-point flow and heat transfer of a Casson fluid towards a stretching sheet. *Zeit Fr Natur* 2012; 67: 70–76.
24. Mustafa M, Hayat T, Pop I, et al. Unsteady boundary layer flow of a Casson fluid due to an impulsively started moving flat plate. *Heat Transfer-Asian Res* 2011; 40: 563–576.
25. Sparrow EM and Lin SH. Laminar heat transfer in tubes under slip-flow conditions. *ASME J Heat Transfer* 1962; 84: 363–639.
26. Inman RM. Heat transfer for laminar slip flow of a rarefied gas in a parallel plate channel or a circular tube with uniform wall temperature. *NASA Technical Report*, D-2213, 1964.
27. Larrode FE, Housiadas C and Drossinos Y. Slip-flow heat transfer in circular tubes. *Int J Heat Mass Transfer* 2000; 43: 2669–2680.
28. Spillane S. *A study of boundary layer flow with no-slip and slip boundary conditions*. Ireland: PhD Thesis, Dublin Institute of Technology, 2007.
29. Crane LJ and McVeigh AG. Slip flow on a microcylinder. *Z Angew Math Phys* 2010; 61(3): 579–582.
30. Ameel TA, Barron RF, Wang XM, et al. Laminar forced convection in a circular tube with constant heat flux and slip flow. *Microscale Thermophys Eng* 1997; 1: 303–320.
31. Yu SP and Ameel TA. Slip-flow convection in isoflux rectangular microchannel. *ASME J Heat Transfer* 2002; 124: 346–355.
32. Crane LJ and McVeigh AG. Uniform slip flow on a cylinder. *PAMM: Proc Appl Math Mech* 2010; 10: 477–478.
33. Anwar Bég O, Zueco J and Lopez-Ochoa LM. Network numerical analysis of optically thick hydromagnetic slip flow from a porous spinning disk with radiation flux, variable thermophysical properties, and surface injection effects. *Chem Eng Commun* 2011; 198: 360–384.
34. Wang CY and Ng C-O. Slip flow due to a stretching cylinder. *Int J Non-Linear Mech* 2011; 46: 1191–1194.
35. Wang CY. Stagnation flow on a cylinder with partial slip—an exact solution of the Navier–Stokes equations. *IMA J Appl Math* 2007; 72: 271–277.

36. Yih KA. Effect of blowing/suction on MHD-natural convection over horizontal cylinder: UWT or UHF. *Acta Mech* 2000; 144: 17–27.
37. Keller HB. A new difference method for parabolic problems. In: J Bramble (ed.) *Numerical methods for partial differential equations*. New York: Academic Press, 1970, pp.327–350.
38. Prasad VR, Vasu B and Anwar Bég O. *Thermo-diffusion and diffusion-thermo effects on boundary layer flows*. Saarbrucken, Germany: Lambert Academic Publishing, 2011.
39. Prasad VR, Vasu B, Anwar Bég O, et al. Thermal radiation effects on magnetohydrodynamic free convection heat and mass transfer from a sphere in a variable porosity regime. *Commun Nonlinear Sci Numer Simul* 2012; 17: 654–671.
40. Prasad VR, Vasu B, Prashad R, et al. Thermal radiation effects on magneto-hydrodynamic heat and mass transfer from a horizontal cylinder in a variable porosity regime. *J Porous Media* 2012; 15: 261–281.
41. Vasu B, Prasad VR, Anwar Bég O, et al. Numerical analysis of magnetohydrodynamic nonlinear convection heat and mass transfer from a sphere in a non-Darcian variable porosity medium. *Int J Appl Math Mech* 2010; 6: 64–111.
42. Anwar Bég O, Prasad VR, Vasu B, et al. Free convection heat and mass transfer from an isothermal sphere to a micropolar regime with Soret/Dufour effects. *Int J Heat Mass Transfer* 2011; 54: 9–18.
43. Anwar Bég O, Gorla RSR, Prasad VR, et al. Computational study of mixed thermal convection nanofluid flow in a porous medium, In: *12th UK National Heat Transfer Conference*, West Yorkshire, UK, 30/31 August to 1 September, University of Leeds, 2011.
44. Bachok N, Ishak A and Pop I. Flow and heat transfer over a rotating porous disk in a nanofluid. *Physica B* 2011; 406: 1767–1772.
45. Molla MM and Hossain MA. Effects of chemical reaction, heat and mass diffusion in natural convection flow from an isothermal sphere with temperature dependent viscosity. *Int J Comput Aided Eng Softw* 2006; 23: 840–857.
46. Chang TB, Mehmood A, Anwar Bég O, et al. Numerical study of transient free convective mass transfer in a Walters-B viscoelastic flow with wall suction. *Commun Nonlinear Sci Numer Simul* 2011; 16: 216–225.
47. Merkin JH. Free convection boundary layers on cylinders of elliptic cross section. *J Heat Transfer* 1977; 99: 453–457.
48. Ajadi SO, Adegoke A and Aziz A. Slip boundary layer flow of non-Newtonian fluid over a flat plate with convective thermal boundary condition. *Int J Nonlinear Sci* 2009; 8: 300–306.
49. Aziz A. Hydrodynamic and thermal slip flow boundary layers over a flat plate with constant heat flux boundary condition. *Commun Nonlinear Sci Numer Simul* 2010; 15: 573–580.
50. Debaste F, Kegelaers Y, Ben Hamor H, et al. Contribution to the modelling of chocolate tempering. In: *Proceedings of the European Congress of Chemical Engineering (ECCE-6)*, Copenhagen, Denmark, 16–20 September 2007.

## Appendix

### Notation

| | |
|---|---|
| $a$ | radius of the cylinder |
| $C_f$ | skin friction coefficient |
| $S_f$ | non-dimensional velocity slip parameter |
| $S_T$ | non-dimensional thermal slip parameter |
| $f$ | non-dimensional steam function |
| $g$ | acceleration due to gravity |
| $Gr$ | Grashof number |
| $N_0$ | velocity slip factor |
| $K_0$ | thermal slip factor |
| $Nu$ | local Nusselt number |
| $Pr$ | Prandtl number |
| $T$ | temperature |
| $u$, $v$ | non-dimensional velocity components along the $x$- and $y$-directions, respectively |
| $x$, $y$ | non-dimensional Cartesian coordinates along and transverse to cylinder surface |
| $\alpha$ | thermal diffusivity |
| $\beta$ | non-Newtonian (rheological) Casson parameter |
| $\Lambda$ | co-efficient of thermal expansion |
| $\Phi$ | azimuthal coordinate |
| $\eta$ | dimensionless radial coordinate |
| $\mu$ | dynamic viscosity |
| $v$ | kinematic viscosity |
| $\theta$ | non-dimensional temperature |
| $\rho$ | density of fluid |
| $\xi$ | dimensionless tangential coordinate |
| $\psi$ | dimensionless stream function |

### Subscripts

| | |
|---|---|
| $w$ | conditions on the wall |
| $\infty$ | free stream conditions |